

**Supplementary Information for**  
**Modulating Charge Density Wave Order in a *1T*-TaS<sub>2</sub>/Black**  
**Phosphorus Heterostructure**

*Ziying Wang<sup>1,2†</sup>, Leiqiang Chu<sup>1,2†</sup>, Linjun Li<sup>4</sup>, Ming Yang<sup>5</sup>, Junyong Wang<sup>2,3</sup>,  
Goki Eda<sup>1,2,3</sup>, Kian Ping Loh<sup>1,2\*</sup>*

<sup>1</sup>Department of Chemistry, National University of Singapore, Singapore, 117543

<sup>2</sup>Centre for Advanced 2D Materials, National University of Singapore, Singapore,  
117546

<sup>3</sup>Department of Physics, National University of Singapore, Singapore, 117542

<sup>4</sup>State Key Laboratory of Modern Optical Instrumentation, College of Optical  
Science and Engineering, Zhejiang University, Hangzhou, China 310027

<sup>5</sup>Institute of Materials Research and Engineering, Agency for Science Technology  
and Research, 2 Fusionopolis Way, Singapore 138634

**Corresponding Author**

\*Email: [chmlhkp@nus.edu.sg](mailto:chmlhkp@nus.edu.sg) Phone: (65) 6516 2658

## Table of Content

1.	Sample preparation and experimental methods .....	3
2.	Activation energy of conductance oscillations.....	7
3.	Coulomb peak line shape analysis .....	8
4.	Angle dependent Raman spectrum of BP/ <i>1T</i> -TaS <sub>2</sub> heterostructure	10
5.	Polarized Raman scattering intensities of the BP/ <i>1T</i> -TaS <sub>2</sub> heterostructure .....	11
6.	Parallel resistance extraction .....	12
7.	Control experiments: Raman and transport characterization of pure <i>1T</i> -TaS <sub>2</sub> and BP. ....	13
8.	First-Principles Calculations.....	19
	Reference .....	21

## 1. Sample preparation and experimental methods

### *Fabrication of BN/IT-TaS<sub>2</sub>/BP devices and conductance oscillations*

#### *measurement details*

All the exfoliation and transfer process were done in an Ar-filled glove box with both O<sub>2</sub> and H<sub>2</sub>O level below 1 ppm. Hexagonal-boron nitride (h-BN) crystal was deposited onto silicon substrate with 300 nm SiO<sub>2</sub> following the standard micromechanical exfoliation. Flakes of approximately 20 nm were identified and selected as substrate with an optical microscope. *IT*-TaS<sub>2</sub> flakes were exfoliated on a PDMS stamp and the flake with a thickness of ~8 nm was transferred onto the BN substrate with the transfer stage. Afterwards a layer of ~20 nm BP flake of thin rectangle shape was transferred on the centre of *IT*-TaS<sub>2</sub> flake. Metal contacts were fabricated on the heterostructure followed by a standard E beam lithography method. The electrodes were arranged in Hall-bar shape and in vicinity to BP. Cr/gold (3/80 nm) were thermally evaporated to form electrodes. The lift-off process was carried out in acetone solution in a glove box. We fabricated two kinds of devices, BN/*IT*-TaS<sub>2</sub>/ BP and BN/*IT*-TaS<sub>2</sub> to directly see BP's effect. After the device was completed, another BN flake was transferred to protect the device from degradation. Finally, the device was wire-bonded to a chip carrier and loaded into the He<sup>4</sup> cryostat chamber for low temperature transport measurements.

For field effect measurements in this work, a dc back gate voltage,  $V_g$ , was applied to tune the carrier densities in *IT*-TaS<sub>2</sub>. The channel current  $I_{sd}$  was

monitored with constant channel voltage  $V_{sd}$  and sweeping  $V_g$ . To eliminate noise disturbance in conductance oscillations measurement, we used both alternating current (ac) and direct current (dc) to measure the field gate effect and found that the conductance oscillations were not distinguishable. Besides, we conducted measurements using 4-probe and 2-probe method and observed no significant differences. As can be seen from Fig S1, the conductance peaks are slightly attenuated in the 2 probe method, but the peak positions remain same. The extracted contact resistance is around 20 K $\Omega$  with little gate dependence. It is relatively small compared to the resistance of sample (40 K $\Omega$ ), so the outcome of 4 probe and 2 probe measurements are similar.

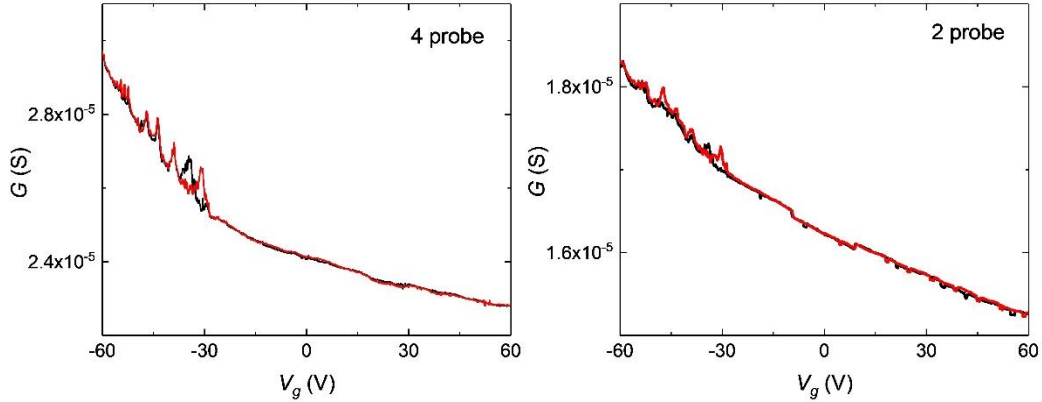


Figure S1 Conductance peaks of BP/IT-TaS<sub>2</sub> measured by four-probe and two-probe method.  $T=1.5$  K,  $V_{sd}=3$  mV.

#### *Fabrication of BN/BP/IT-TaS<sub>2</sub>/BN devices*

As CDW transitions in IT-TaS<sub>2</sub> are thickness dependent<sup>1</sup>, it is necessary to characterize pristine IT-TaS<sub>2</sub> of similar thickness when we compare the influence of BP versus a more “inert” substrate such as BN. We fabricated BN/BP/IT-

TaS<sub>2</sub>/BN and BN/*IT*-TaS<sub>2</sub>/BN devices from one TaS<sub>2</sub> flake—part of *IT*-TaS<sub>2</sub> flake was on BP and part was on BN, to directly illuminate the substrate effect. The flake exfoliation and transfer methods used in fabrication of BN (~20 nm)/BP (~20 nm)/*IT*-TaS<sub>2</sub> (5~8 nm)/BN devices are same with those described in previous section. The stacking sequence here is BN-BP-TaS<sub>2</sub>. To perform angle dependent transport measurements, the heterostructure was etched with deep reactive ion etching (DRIE) into a series of rectangular bars rotated at 30° degree from each other. Afterwards, two edge-contacts were fabricated on each rectangular bar to form an independent device. Cr/gold (2/80 nm) were thermally evaporated to form electrodes. The lift-off process was carried out in a glove box and finished within a few minutes. After the devices were completed, another BN flake was transferred to cover the device to protect the side contact electrodes from degradation.

A schematic illustration of the heterostructure is shown in Fig. S2a. Figure S1b shows the BN/*IT*-TaS<sub>2</sub>/BN and BN/BP (~20 nm)/*IT*-TaS<sub>2</sub> (~8 nm)/BN (~20 nm) devices fabricated on one TaS<sub>2</sub> flake. In Fig. 2b right panel, in the upper region the device structure is BN/BP/*IT*-TaS<sub>2</sub>/BN and in the lower region the structure is BN/*IT*-TaS<sub>2</sub>/BN. In this configuration, the thickness and crystal quality of TaS<sub>2</sub> with and without BP are equivalent, and any differences should arise solely from interfacial effects.

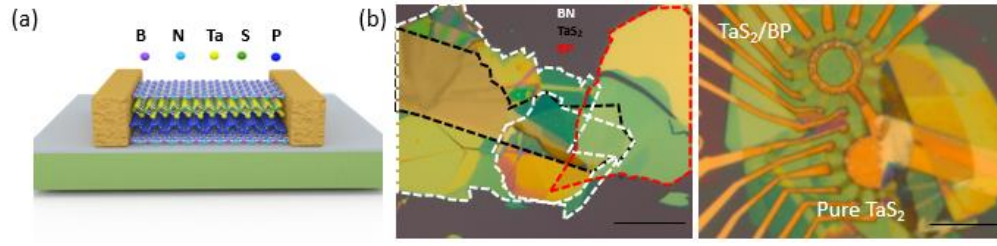


Figure S2. (a) Side view of BN/BP/1T-TaS<sub>2</sub>/BN heterostructure. (b) Optical images of the BN/BP/1T-TaS<sub>2</sub>/BN heterostack before and after electrical contact, respectively. Scale bars in left and right are 20  $\mu\text{m}$  and 3  $\mu\text{m}$ , respectively. The bar-shaped devices with side metal contact are rotated 30° from each other. Devices in upper region have the structure of BN/1T-TaS<sub>2</sub>/BP/BN, and lower devices are BN/1T-TaS<sub>2</sub>/BN.

#### *STM sample preparation and experimental details*

A silicon substrate coated with 100 nm Au film was used as substrate for STM study. First a layer of BP flake was exfoliated and transferred on the substrate. Afterwards, a bilayer 1T-TaS<sub>2</sub> flake was transferred on BP. The bilayer flake was connected to a big bulk TaS<sub>2</sub> flake which was used as reference to locate the thin area under the CCD camera mounted on the STM chamber. The STM study was performed in an Omicron ultrahigh vacuum (UHV) system equipped with a low temperature STM. To avoid surface contamination or deterioration in air, the freshly fabricated 1T-TaS<sub>2</sub>/BP was quickly transferred into an UHV system with the base pressure below  $5 \times 10^{-10}$  mbar. STM images taken on Au(111) substrate were used as reference for tip calibration.

### *Experimental details for Raman measurement*

The heterostructure of BN/BP/1T-TaS<sub>2</sub>/BN for Raman measurements was prepared following the method described in previous sections. Raman measurement was carried out with 633 nm wavelength He–Ne wavelength laser and 2400/mm grating. To avoid thermal degradation of sample, the laser power was controlled below 100  $\mu$ W with an integration time of 10 seconds. We used a homemade rotatable chamber in which angle-dependent low temperature Raman can be conducted. During measurements, we rotated the sample stage at angles of 15 or 30° to tune the direction between incident laser polarization and crystal direction and kept all other parameters same. Liquid nitrogen is used to keep the system at 77 K. For polarized Raman measurements, the polarization orientation of Raman signal is controlled by rotating the analyser in front of the entrance slit of the spectrometer to be either parallel or perpendicular to the incident light.

## **2. Activation energy of conductance oscillations**

We extract the activation energy of conductance maximum and minimum of a peak as Fig. S3 shows. In Fig. S3a, the peak and valley values of conductance peak 1 and 2 (highlighted by the black arrow in Fig. 3) are plotted as a function of temperature. Figure S3b displays the extracted maximum and minimum values of conductance oscillations in another device (named as device 2). The grey solid lines are linear fittings of the data points according to the equation,

$$G \propto \exp(-E_{act}/kT) \quad (5-1)$$

where  $k$  is the Boltzmann constant at a value of  $8.62 \times 10^{-5}$  eV/K. The activation energy for device 1 and 2 are 0.22 and 0.46 meV, respectively. At the temperature of 1.5 K, the thermal energy is around 0.195 meV, which is smaller than the activation energy.

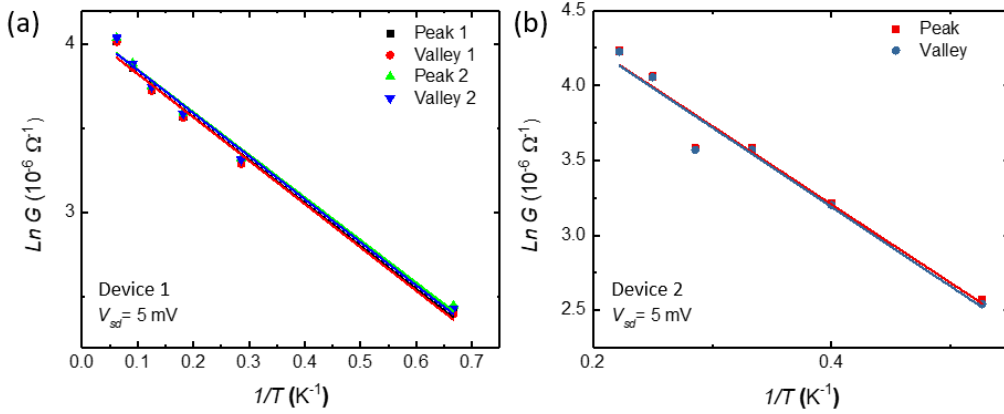


Figure S3 **Log G vs  $T^{-1}$  of extracted peak and valley values of conductance peaks.** **a** Extracted conductance maximum and minimum value from peak 1 and 2 (showed by arrow in Fig. 5) . **b** Extracted maximum and minimum value of a conductance peak from another device. All conductance maximum and minimum are temperature dependent, which increases with temperature. The grey solid lines are linear fitting of data.

### 3. Coulomb peak line shape analysis

The line shape of the Coulomb peaks reflects coupling strengths between quantum dot and electrodes<sup>2-4</sup>. In weak coupling regime, Coulomb oscillations can be classified into quantum (resonant tunnelling) and classical regimes according to different temperature ranges. In the quantum regime where  $kT \leq \Delta E$ , only a single energy level in the quantum dot participates in the conduction. In the classical regime where  $\Delta E \leq kT$ , a continuum of energy levels in the quantum dot take part in the conduction.



$$\frac{G}{G_{max}} = \frac{\Delta E}{4kT} \cosh^{-2} \left( \frac{\delta}{2kT} \right), \text{ if } h\Gamma \leq kT \leq \Delta E, e^2/C, \text{ quantum regime} \quad (2)$$

$$\frac{G}{G_{max}} = \frac{1}{2} \cosh^{-2} \left( \frac{\delta}{2.5kT} \right), \text{ if } h\Gamma, \Delta E \leq kT \leq e^2/C, \text{ classical regime} \quad (2)$$

$$G = \frac{2e^2}{h} \frac{(h\Gamma)^2}{(h\Gamma)^2 + \delta^2}, \text{ if } T = 0, \frac{e^2}{C} \leq h\Gamma, \Delta E, \text{ strong coupling regime} \quad (3)$$

where  $G$  is the conductance of peak,  $G_{max}$  is the maximum conductance at high temperature,  $k$  is the Boltzmann's constant,  $\Gamma$  is the tunnelling rate through the barrier,  $\delta$  is the horizontal distance to peak centre,  $\Delta E$  is the average energy level spacing, and  $e^2/C$  is the charging energy. The coulomb peaks in strong coupling regime expressed in Eq. (3) has the Lorentzian line shape.

Fig S4 a and b shows the full width at half maximum (FWHM) and peak height as a function of temperature, respectively. As can be seen, the FWHM increases linearly with temperature, whereas the peak amplitudes are almost constant with temperature. The trend of FWHM and peak height suggests the Coulomb oscillations are within the classical regime, where a series of energy levels in the isolated segments participate in tunnelling<sup>2-4</sup>.

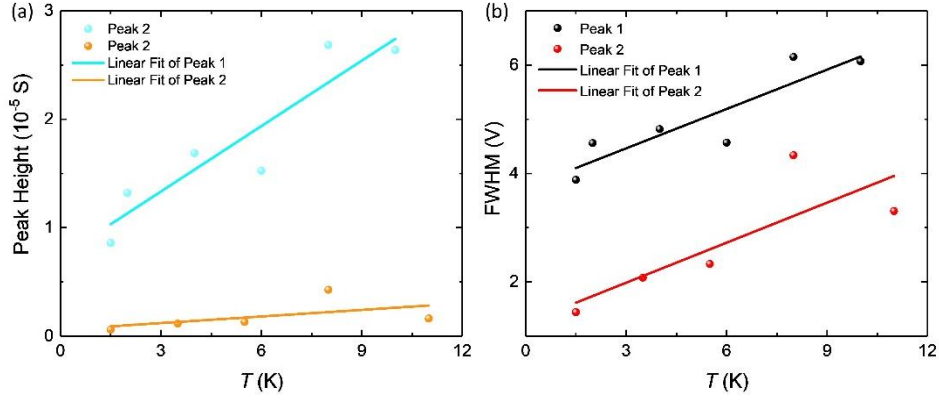


Figure S4 Peak analysis with CB model. (a) Peak height of two independent peaks (1 and 2) as a function of temperature. The solid lines are the linear fits. (b) The FWHM of Peak 1 and 2 are shown as a function of temperature.

#### 4. Angle dependent Raman spectrum of BP/1T-TaS<sub>2</sub> heterostructure

Figure S5 shows the angle-resolved Raman spectrum of BN/BP/1T-TaS<sub>2</sub>/BN at 77 K with a sample rotation angle range of 180°, at a step of 30°. The phonon modes between 220 and 400 cm<sup>-1</sup> are ascribed to the  $E_g$  and  $A_{1g}$  optical modes of TaS<sub>2</sub> and have their origins in the vibrations of the sulphur atoms, and the modes between 60 and 120 cm<sup>-1</sup> are ascribed to the acoustic and interlayer modes from the vibrations of the tantalum atoms<sup>5-7</sup>. Low-frequency (below 120 cm<sup>-1</sup>) folded-back acoustic Raman modes<sup>5, 7-9</sup> are well resolved, indicating 1T-TaS<sub>2</sub> is in C phase<sup>7, 10</sup>.

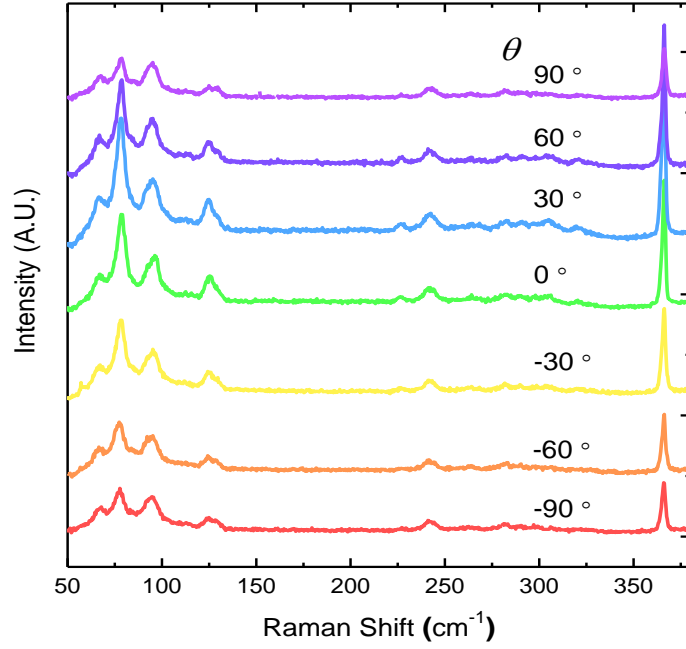


Figure S5. Raman spectra taken at 77 K with different rotation angles of BN/*IT*-TaS<sub>2</sub>/BP/BN samples with a 633-nm laser ( $\theta$  represents the rotation angle of the sample).

## 5. Polarized Raman scattering intensities of the BP/*IT*-TaS<sub>2</sub> heterostructure

To probe the anisotropy of Raman modes of BP/ TaS<sub>2</sub>, angle dependent Raman measurements with polarised laser are conducted, as is shown in Fig. S6. The 2D images show that in both parallel  $\bar{z}(xx)z$  and cross-polarized  $\bar{z}(xy)z$  configuration, TaS<sub>2</sub> shows anisotropic Raman responses that are correlated with the  $A_g^1$  mode of BP.

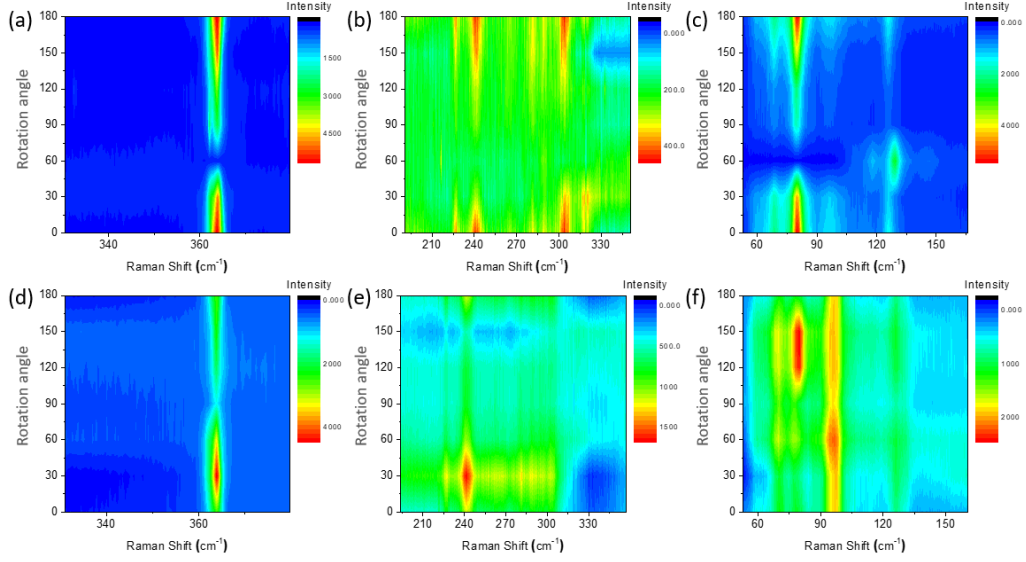


Figure S6 **Polarized Raman scattering intensities of the BN/BP/1T-TaS<sub>2</sub>/BN heterostructure.** 2D images of Raman intensity at different rotation angles of BP  $A_g^1$  mode (a) and 1T-TaS<sub>2</sub> modes (b, c) in parallel polarization configuration. 2D images of Raman intensity at different rotation angles of BP  $A_g^1$  mode (d) and 1T-TaS<sub>2</sub> modes (e, f) in cross-polarized configuration.

## 6. Parallel resistance extraction

In the heterostructure of BP/TaS<sub>2</sub>, the parallel resistance of 1T-TaS<sub>2</sub> follows equation of resistors connected in parallel:  $\frac{1}{R_{total}} = \frac{1}{R_{BP}} + \frac{1}{R_{TaS_2}}$ , where  $R_{total}$  is the as measured resistance;  $R_{BP}$  is resistance of BP, taken from BN encapsulated BP devices (see Figure. S12). We included a conductance anisotropy ratio of 4 of BP in calculations.

## 7. Control experiments: Raman and transport characterization of pure *1T*-TaS<sub>2</sub> and BP.

Following the same investigation method and experimental procedures in heterostructure of BP/*1T*-TaS<sub>2</sub>, we carry out Raman and transport characterization of BN encapsulated pure *1T*-TaS<sub>2</sub> and BP.

### *Raman characterization*

To probe the isotropic nature of CDW of pure *1T*-TaS<sub>2</sub>, angle-resolved Raman spectrum is collected at 77 K, as is shown in Fig. S7a. In Fig. S7b, 2D colour image of angle dependent Raman response is plotted. The Raman intensities and shifts are not varying as the angle changes, which verifies that the phonon vibrations are isotropic in pure *1T*-TaS<sub>2</sub>.

BP is an anisotropic 2D material that has zigzag and armchair direction. Angle dependent Raman spectrum collected at room temperature is shown in Fig. S7c. The intensities of the three typical modes at 361 ( $A_g^1$ ), 438 ( $B_{2g}$ ) and 466 ( $A_g^2$ ) cm<sup>-1</sup> are obviously angle dependent. From the 2D plot (Fig. S7d),  $A_g^1$  and  $A_g^2$  show a periodicity of  $\pi$  with one relatively larger local maximum (armchair) and one smaller (zigzag) local maximum across  $\pi$ . Raman responses of  $A_g^1$  and  $A_g^2$  modes have the same phase and periodicity in the 2D image. Our Raman results are comparable with the literatures<sup>11</sup>.

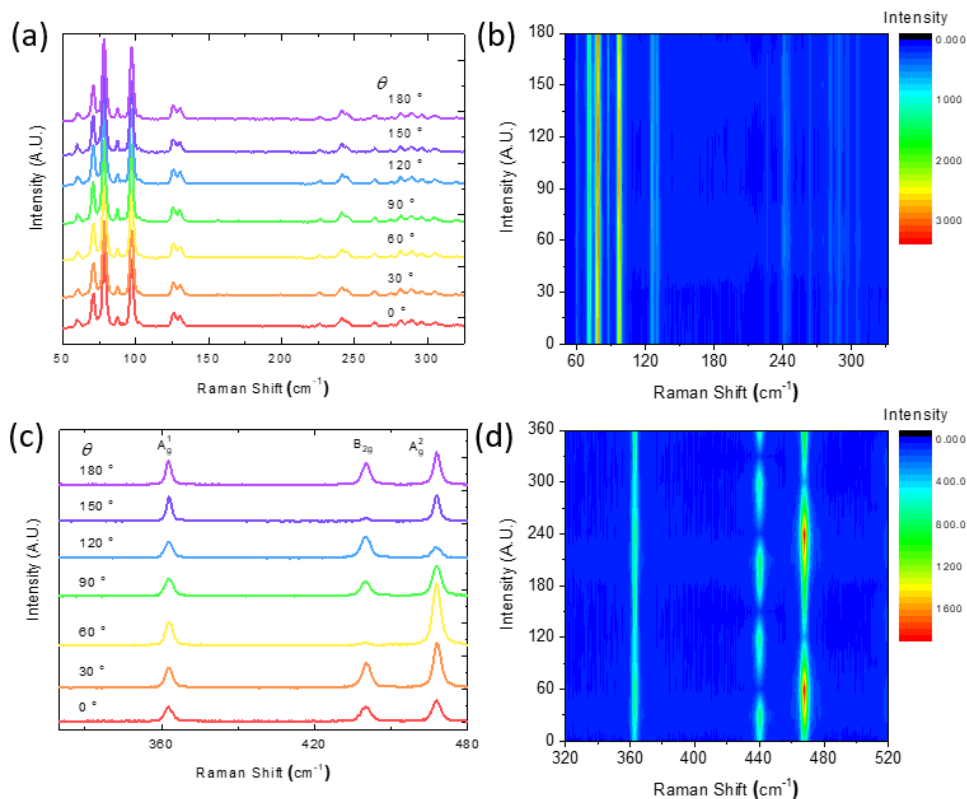


**Figure S7 Angle dependent Raman characterisation of the BN encapsulated 1T-TaS<sub>2</sub> and BP samples in the parallel configuration.** **a** Angle dependent Raman spectrum of BN/1T-TaS<sub>2</sub>/BN sample collected at 77 K with 633 nm laser. **b** 2D image of Raman response of 1T-TaS<sub>2</sub>. **c** Angle dependent Raman spectrum of BN/BP/BN sample collected at 285 K with 633 nm laser. **d** 2D image of Raman response of BP.

### *Charge transport characteristic*

The transfer characteristics of BN encapsulated few layer 1T-TaS<sub>2</sub> is showed in Fig. S8. Pure TaS<sub>2</sub> shows no obvious conductance oscillations, and there is no coulomb diamond structure in the 2D image (Fig. S8b). Besides, the transfer curves show the p-type behavior of 1T-TaS<sub>2</sub>. The on/off ratios at both 1.5 K is less than 2, implying little gate modulation effect.

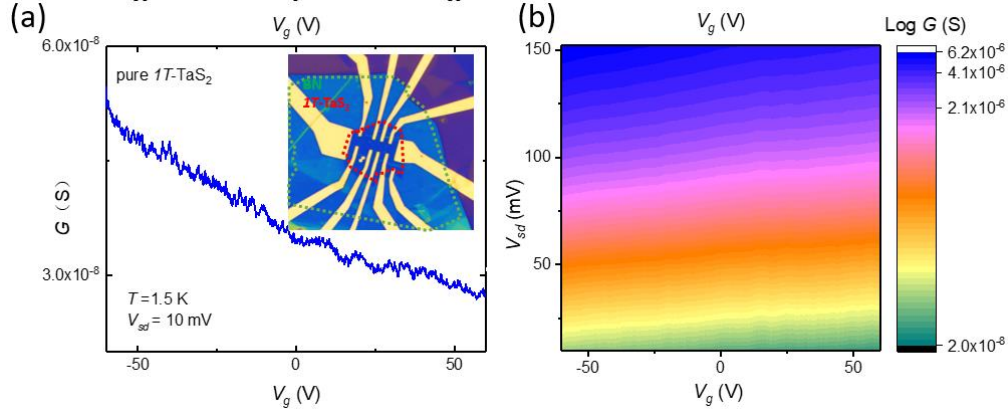


**Figure S8.** Conductance as a function of gate voltage in BN/1T-TaS<sub>2</sub>/BN device. (a) Field effect modulated conductance curve from BN/1T-TaS<sub>2</sub> device under a small bias of  $V_{sd} = 10$  mV at 1.5 K. No obvious peaks are observed. Inset: optical image of a completed BN/1T-TaS<sub>2</sub>/BN device. (b) 2D color map of conductance at different  $V_{sd}$  as a function of  $V_g$ , plotted in logarithmic scale, from a BN/1T-TaS<sub>2</sub> device.

Basic charge transport properties of BP device are showed in Fig. S9. Ohmic contact to crystal is indicated by the linear  $I$ - $V$  curves (Fig. S9b) at different temperatures, due to the well-aligned work function of metal contact (2 nm Cr/ 60 nm Au) with the valence band of BP. Figure S9c shows temperature dependent transfer curves from 2 K to 250K. BP shows p-type dominated ambipolar behavior, with the on/off ratio reaching 4 orders at room temperature and 7 orders at low temperature<sup>12</sup>. The light blue box separates the low-mobility (I) and high-mobility (II) regions. Here we deduce the mobility and carrier concentration in region II to compare the quality of our BP device to those reported previously. The field effect mobility  $\mu_{FE}$  can be extracted in the linear region with the formula<sup>12</sup>

$$\mu_{FE} = \frac{L}{W} C_{ox}^{-1} (dG/dV_g) \quad (6)$$

where  $L$  and  $W$  are length and width of the channel, respectively,  $G$  is the conductance,  $C_{ox} = 12.1$  nF is the capacitance of 285 nm  $\text{SiO}_2$ <sup>9</sup>. The extracted  $\mu_{FE}$  reaches  $1600 \text{ cm}^2\text{V}^{-1}\text{s}^{-1}$  at 2K. The carrier concentration can be estimated as the method showed in Fig. S10:

$$n \approx \frac{C_{ox}|V_g - V_0|}{e} \quad (7)$$

The extracted carrier concentration  $n$  is about  $1.76 \times 10^{12} \text{ cm}^{-2}$  at 2 K. Both the  $\mu_{FE}$  and  $n$  values are comparable with those reported in high quality BP devices, where mobility and carrier concentration reach  $2000 \text{ cm}^2\text{V}^{-1}\text{s}^{-1}$  and  $10^{12} \text{ cm}^{-2}$ <sup>13-14</sup>.

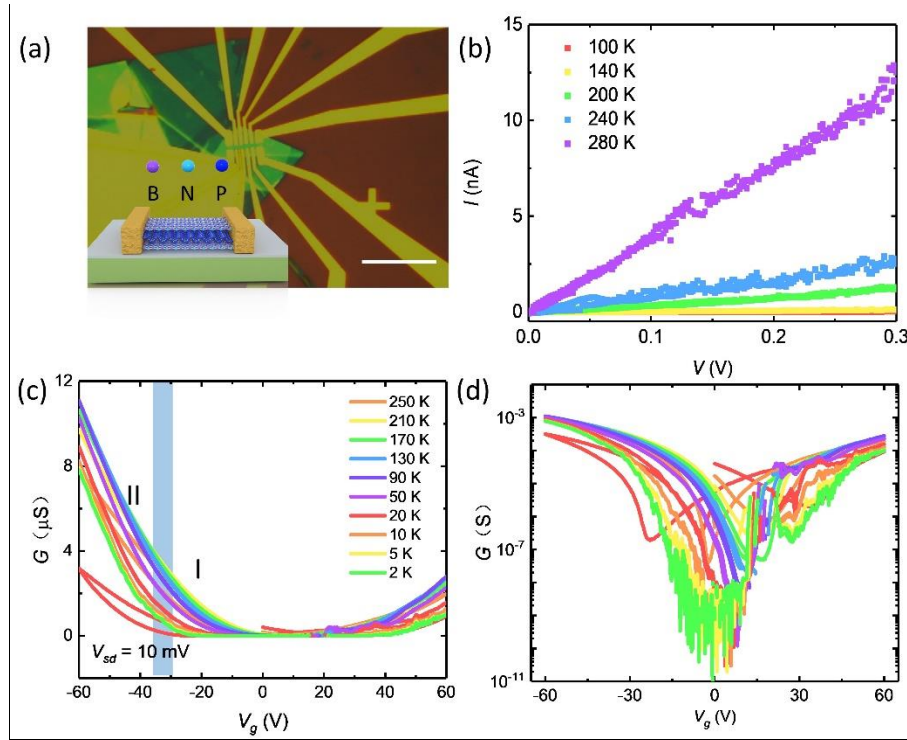


**Figure S9 Basic charge transport of the BN encapsulated BP device.** **a** Optical images of the completed BN/BP/BN device. Scale bar: 10 μm. Inset: side view of the van der Waals heterostructure of BN/ BP/BN. **b** DC  $I$ - $V$  characterization at a range of temperatures. The linear  $I$ - $V$  curves show ohmic contact to crystals. **c**



Conductance as a function of  $V_g$  collected from 250 K to 2K, under a constant source-drain voltage of 10 mV. BP shows p-type and ambipolar behaviour in gate modulated conductance and the on/off ratio is as large as 4 orders at 250 K and 7 orders at 2 K. **d** The same figure in panel c plotted in logarithmic scale.

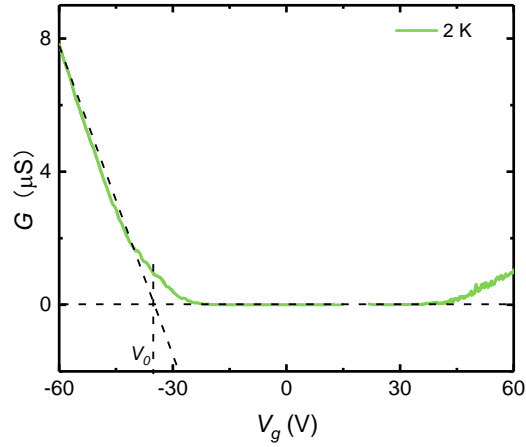


Figure S10 Estimation of charge carrier concentration from field effect modulation in BN encapsulated BP device.

#### *Temperature dependent charge transport*

Figure S11 shows the angle-dependent resistance plots with respect to temperature for pure  $1T$ -TaS<sub>2</sub>. The resistance jump of more than one order of magnitude between 140 and 150 K indicates the NC-to-C phase transition. The hysteresis loop between cooling and warming has a temperature range of approximately 120 K. The NC to C transition shows no difference in all three directions in pure  $1T$ -TaS<sub>2</sub>. Therefore, the NC-to-C phase transition is isotropic in  $1T$ -TaS<sub>2</sub> supported on BN, as would be expected of a pristine sample on an inert substrate.

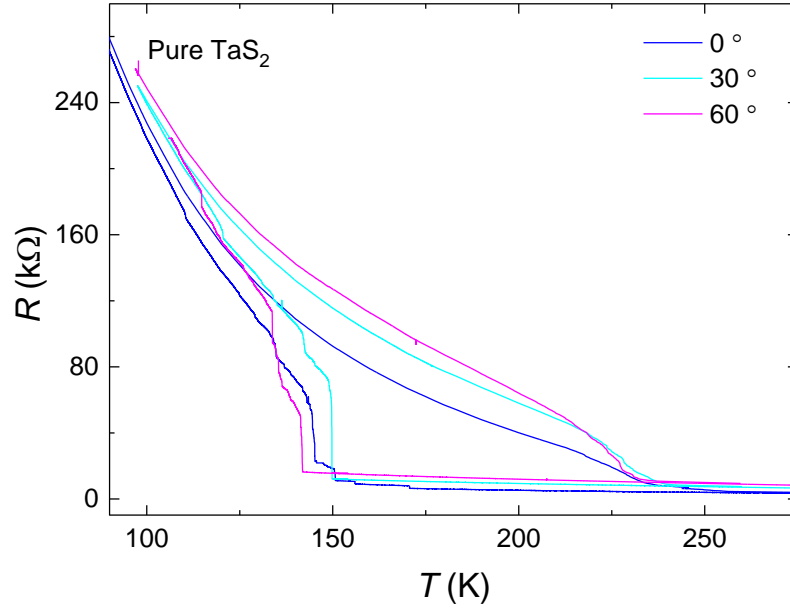


Figure S11. Temperature dependent resistance of BN encapsulated  $1T$ -TaS<sub>2</sub> (~5 nm) along three angles. The NC-to-C phase transition is isotropic in  $1T$ -TaS<sub>2</sub> supported on BN.

For BN encapsulated BP device, the temperature dependent charge transport data at 0  $V_g$  and -60  $V_g$  are showed in Fig. S12 a and b, respectively. Under 0  $V_g$ , BP behaves as a normal semiconductor, with resistance increasing from  $10^5$  at room temperature to  $10^{11} \Omega$  at 2 K. These numbers show that the resistance of BP is orders of magnitude higher than that of  $1T$ -TaS<sub>2</sub> over the whole temperature range. In contrast, at -60  $V_g$ , resistance of BP does not vary much as temperature changes. BP behaves like a metal above 150 K and a metal to insulator transition occurs around 100 K, after which the resistivity slowly increases. This is a typical behaviour of weak localization of BP when BP is highly doped<sup>15-18</sup>.

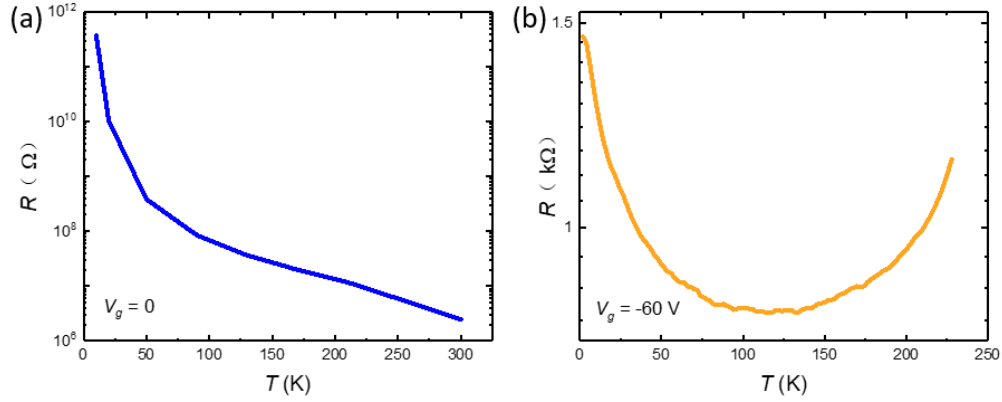


Figure S12 Resistivity as a function of temperature of BN/BP/BN device at 0 (a) and  $-60$  V gate voltage (b).

## 8. First-Principles Calculations

All the density-functional theory (DFT) calculation were performed using the Vienna ab initio simulation package (VASP5.4.4.18) with projector augmented wave (PAW) pseudopotentials<sup>19-20</sup>, in which the exchange-correlation interaction was treated by Perdew-Burke-Ernzerhof (PBE) parameterized functionals<sup>21</sup>. The cut-off energy for the plane-wave basis set was set to 500 eV. The CDW structure of  $1T$ -TaS<sub>2</sub> monolayer was modelled by using  $(\sqrt{13} \times \sqrt{13} \times 1)$  supercell with 39 atoms. For all TaS<sub>2</sub> monolayer and hybrid structures, vacuum layers with a thickness of 15 Å were applied normal to TaS<sub>2</sub> layer. To study the interfacial interaction between TaS<sub>2</sub> and BP substrate,  $(1 \times 3 \sqrt{3})$   $1T$ -TaS<sub>2</sub> monolayer was placed on  $(1 \times 4)$  BP bi-layers, where about 1.8% compressive and tensile strain are found along zigzag and armchair direction of the TaS<sub>2</sub> layers, respectively. van der Waals (vdWs) interaction in interface structure was included

using Grimme's DFT-D3 method<sup>22</sup>. The first Brillouin zone of *1T*-TaS<sub>2</sub>, *1T*-TaS<sub>2</sub> with CDW structure, and TaS<sub>2</sub>/BP interface structure was sampled by using  $\Gamma$ -centered  $15 \times 15 \times 1$ ,  $6 \times 6 \times 1$ , and  $15 \times 3 \times 1$  k-point meshes, respectively. The energy and force on each atom for all calculations were optimized smaller than  $1.0 \times 10^{-6}$  eV and 0.01 eV/Å, respectively. Based on these settings, the calculated lattice constant of *1T*-TaS<sub>2</sub> monolayer is 3.38 Å. The calculated band structure for the pristine *1T*-TaS<sub>2</sub> monolayer and CDW structure are shown in Figure S13 (a) and (b). All these results are consistent with previous calculations<sup>23</sup>.

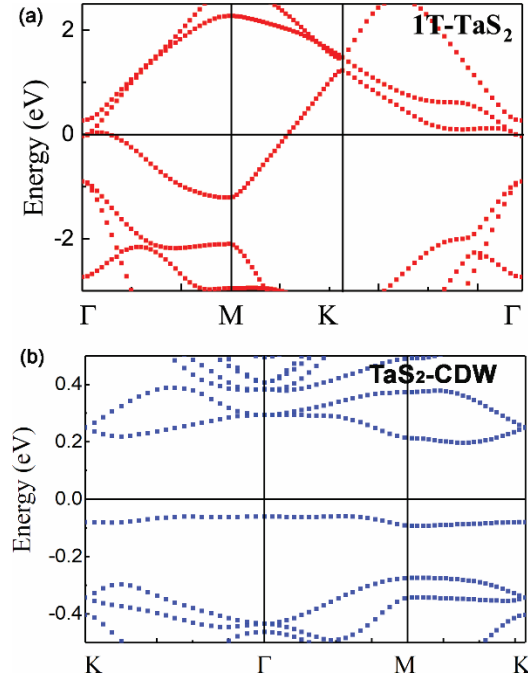


Figure S13: The band structure of (a) pristine *1T*-TaS<sub>2</sub> monolayer and (b) TaS<sub>2</sub> supercell with CDW structure.

## Reference

- (1) Tsen, A. W.; Hovden, R.; Wang, D.; Kim, Y. D.; Okamoto, J.; Spoth, K. A.; Liu, Y.; Lu, W.; Sun, Y.; Hone, J. C.; Kourkoutis, L. F.; Kim, P.; Pasupathy, A. N., Structure and control of charge density waves in two-dimensional 1T-TaS<sub>2</sub>. *Proc Natl Acad Sci U S A* **2015**, *112* (49), 15054-9.
- (2) Bird, J. P., *Electron transport in quantum dots*. Springer Science & Business Media: 2013.
- (3) Beenakker, C. W. J., Theory of Coulomb-blockade oscillations in the conductance of a quantum dot. *Physical Review B* **1991**, *44* (4), 1646-1656.
- (4) Song, X.-X.; Zhang, Z.-Z.; You, J.; Liu, D.; Li, H.-O.; Cao, G.; Xiao, M.; Guo, G.-P., Temperature dependence of Coulomb oscillations in a few-layer two-dimensional WS<sub>2</sub> quantum dot. *Scientific Reports* **2015**, *5*, 16113.
- (5) Albertini, O. R.; Zhao, R.; McCann, R. L.; Feng, S.; Terrones, M.; Freericks, J. K.; Robinson, J. A.; Liu, A. Y., Zone-center phonons of bulk, few-layer, and monolayer 1T-TaS<sub>2</sub>: Detection of commensurate charge density wave phase through Raman scattering. *Physical Review B* **2016**, *93* (21), 214109.
- (6) Duffey, J. R.; Kirby, R. D.; Coleman, R. V., Raman scattering from 1T-TaS<sub>2</sub>. *Solid State Commun.* **1976**, *20* (6), 617-621.
- (7) Sugai, S.; Murase, K.; Uchida, S.; Tanaka, S., Comparison of the soft modes in tantalum dichalcogenides. *Physica B+C* **1981**, *105* (1), 405-409.
- (8) Uchida, S.; Sugai, S., Infrared and Raman studies on commensurate CDW states in transition metal dichalcogenides. *Physica B+C* **1981**, *105* (1), 393-399.
- (9) Cui, X.; Lee, G.-H.; Kim, Y. D.; Arefe, G.; Huang, P. Y.; Lee, C.-H.; Chenet, D. A.; Zhang, X.; Wang, L.; Ye, F.; Pizzocchero, F.; Jessen, B. S.; Watanabe, K.; Taniguchi, T.; Muller, D. A.; Low, T.; Kim, P.; Hone, J., Multi-terminal transport measurements of MoS<sub>2</sub> using a van der Waals heterostructure device platform. *Nat Nano* **2015**, *10* (6), 534-540.
- (10) Smith, J. E.; Tsang, J. C.; Shafer, M. W., Raman spectra of several layer compounds with charge density waves. *Solid State Commun.* **1976**, *19* (4), 283-286.
- (11) Wu, J.; Mao, N.; Xie, L.; Xu, H.; Zhang, J., Identifying the Crystalline Orientation of Black Phosphorus Using Angle-Resolved Polarized Raman Spectroscopy. *Angew. Chem. Int. Ed.* **2015**, *54* (8), 2366-2369.
- (12) Li, L.; Yu, Y.; Ye, G. J.; Ge, Q.; Ou, X.; Wu, H.; Feng, D.; Chen, X. H.; Zhang, Y., Black phosphorus field-effect transistors. *Nature Nanotechnology* **2014**, *9*, 372.
- (13) Li, L.; Yang, F.; Ye, G. J.; Zhang, Z.; Zhu, Z.; Lou, W.; Zhou, X.; Li, L.; Watanabe, K.; Taniguchi, T.; Chang, K.; Wang, Y.; Chen, X. H.; Zhang, Y.,

- Quantum Hall effect in black phosphorus two-dimensional electron system. *Nature Nanotechnology* **2016**, *11*, 593.
- (14) Li, L.; Ye, G. J.; Tran, V.; Fei, R.; Chen, G.; Wang, H.; Wang, J.; Watanabe, K.; Taniguchi, T.; Yang, L.; Chen, X. H.; Zhang, Y., Quantum oscillations in a two-dimensional electron gas in black phosphorus thin films. *Nature Nanotechnology* **2015**, *10*, 608.
- (15) Simmons, M.; Hamilton, A.; Pepper, M.; Linfield, E.; Rose, P.; Ritchie, D., Weak localization, hole-hole interactions, and the “metal”-insulator transition in two dimensions. *Phys. Rev. Lett.* **2000**, *84* (11), 2489.
- (16) Bergmann, G., Weak localization in thin films: a time-of-flight experiment with conduction electrons. *Physics Reports* **1984**, *107* (1), 1-58.
- (17) Du, Y.; Neal, A. T.; Zhou, H.; Peide, D. Y., Weak localization in few-layer black phosphorus. *2D Materials* **2016**, *3* (2), 024003.
- (18) Long, G.; Xu, S.; Cai, X.; Wu, Z.; Han, T.; Lin, J.; Cheng, C.; Cai, Y.; Wang, X.; Wang, N., Gate-tunable strong-weak localization transition in few-layer black phosphorus. *Nanotechnology* **2017**, *29* (3), 035204.
- (19) Kresse, G.; Furthmüller, J., Efficient iterative schemes for ab initio total-energy calculations using a plane-wave basis set. *Physical review B* **1996**, *54* (16), 11169.
- (20) Kresse, G.; Joubert, D., From ultrasoft pseudopotentials to the projector augmented-wave method. *Physical Review B* **1999**, *59* (3), 1758.
- (21) Perdew, J. P.; Burke, K.; Ernzerhof, M., Generalized gradient approximation made simple. *Phys. Rev. Lett.* **1996**, *77* (18), 3865.
- (22) Wu, X.; Vargas, M.; Nayak, S.; Lotrich, V.; Scoles, G., Towards extending the applicability of density functional theory to weakly bound systems. *The Journal of Chemical Physics* **2001**, *115* (19), 8748-8757.
- (23) Shao, D.; Xiao, R.; Lu, W.; Lv, H.; Li, J.; Zhu, X.; Sun, Y., Manipulating charge density waves in 1 T– TaS<sub>2</sub> by charge-carrier doping: A first-principles investigation. *Physical Review B* **2016**, *94* (12), 125126.